Hindawi
International Journal of Antennas and Propagation
Volume 2019, Article ID 8283236, 12 pages
https://doi.org/10.1155/2019/8283236

Research Article

Compact Microstrip-Based Textile Antenna for 802.15.6 WBAN-UWB with Full Ground Plane

Purna B. Samal,[1] **Ping Jack Soh**,[2] **and Zahriladha Zakaria**[3]

[1]*Electronics and Communication Engineering Department, College of Science and Technology, Rinchending, Phuentsholing, Bhutan*
[2]*Advanced Communication Engineering (ACE) Centre of Excellence, School of Computer and Communication Engineering, Universiti Malaysia Perlis (UniMAP), Pauh Putra Campus, 02600 Arau, Perlis, Malaysia*
[3]*Centre for Telecommunication Research and Innovation (CeTRI), Faculty of Electronic and Computer Engineering, Universiti Teknikal Malaysia Melaka (UTeM), 76100 Melaka, Malaysia*

Correspondence should be addressed to Purna B. Samal; purna.cst@rub.edu.bt

Received 17 October 2018; Revised 12 January 2019; Accepted 21 January 2019; Published 25 March 2019

Academic Editor: Paolo Baccarelli

The paper presents the design and investigation of a flexible all-textile antenna operating in the wireless body area network (WBAN) ultrawideband (UWB) specified by the IEEE 802.15.6 standard. The proposed antenna features an innovative and compact UWB radiator on top of the overall structure with a full ground plane on its reverse side. The radiator, which is based on a microstrip patch combined with multiple miniaturization and broadbanding methods, resulted in a simple topology and a compact size of $39\,\text{mm} \times 42\,\text{mm} \times 3.34\,\text{mm}$ ($0.51 \times 0.55 \times 0.043\lambda$). In comparison to the literature, the proposed structure is considered to be the most compact microstrip-based textile UWB antenna to date featuring a full ground plane. The choice of the commercial textiles is also made based on cost efficiency, ease of accessibility, and ease of fabrication using simple tools. Meanwhile, the full ground plane enables the antenna operation in the vicinity of the human body with minimal body coupling and radiation towards it, ensuring operational safety. Besides its operation in the mandatory channels of the WBAN-UWB low and high bands, the proposed antenna also operates and preserves its performance in five other optional channels of the high band when placed on the body and under bend conditions of 30° and 60°. The proposed antenna successfully achieved the specific absorption rate below the regulated limit specified by the Federal Communications Commission.

1. Introduction

The ultrawideband (UWB) technology introduced by the Federal Communications Commission (FCC) [1] requires a wide operating bandwidth of 7.5 GHz. This requirement triggered widespread research in overcoming the narrowband property of conventional planar antennas for its application. The technology provided a capability for high data rate transmission with low-power spectral densities [2, 3] as compared to a conventional wireless communication system. Due to its immense potential in body-worn communications [4], UWB technology was extended into the application of wireless body area network (WBAN). Based on the recent IEEE 802.15.6 WBAN standard [5], two mandatory UWB channels (low and high bands) can be used for operations. The low band (LB) is divided into three operating channels: 0, 1, and 2, with each channel requiring a bandwidth of 500 MHz and a total required LB bandwidth of 1.5 GHz operating from 3.24 to 4.74 GHz. Channel 1 is the mandatory channel in LB with its operation centered at 3.99 GHz. The high band (HB) consists of eight operating channels from Channel 3 to Channel 10. Similar to LB, each channel requires a bandwidth of 500 MHz, with a total operating bandwidth of 3.99 GHz (from 6.24 GHz to 10.23 GHz). The mandatory channel in HB is Channel 6 centered at 7.99 GHz.

WBAN provides an immense potential in applications such as health monitoring [6, 7], location tracking, and emergency rescue services [8, 9]. Such applications require wireless devices to operate in close proximity to the human body, demanding a requirement for antennas that use flexible materials. This is to ensure conformance to the users' body and ease of integration onto clothing and to guarantee

comfort and safety to users due to their prolonged usage near or on the body. Due to the recent introduction of commercial conductive textiles, antennas for WBAN are increasingly designed and implemented fully using textiles [10, 11]. Besides being easily integrated to clothing, the use of textiles enables a degree of transparency to the users in contrast to conventional worn electronic devices such as smart watches, loggers, trackers, and mobile devices. However, the dielectric properties of the human body poses a challenge to the full implementation of such wearable antennas, as wireless signals from these wearable antennas are very likely to be coupled to the body, resulting in inconsistent or unreliable performance. This calls for a design of textile-based wearable antennas that are not susceptible to any on-body detuning to facilitate reliable WBAN communication.

One of the simplest and yet most effective method to protect the antenna against the effects of detuning caused by the human body (and vice versa) is the use of a full ground plane. Such ground planes, which need to be placed between the radiating element and the human body, are available in specific planar antenna types such as microstrip antennas. Moreover, the planar structure of the antenna is required to ensure proper integration onto the body using textile materials. However, the main limitation of this antenna type is its narrow bandwidth [12, 13], which makes it unsuitable for UWB applications. Broadbanding efforts for microstrip antennas have been previously presented, with a recent work in [14] proposing a microstrip-based UWB textile antenna based on FCC's specifications, from 3.1 to 10.6 GHz, which resulted in minimal backward radiation. Besides its robust performance, the microstrip-based topology also provided safe specific absorption rate (SAR) values, which characterizes the level of electromagnetic absorption by tissues located in the proximity of the antennas [15]. A key factor in achieving the required UWB behavior in [14] is the combined use of various bandwidth enhancement techniques, at the expense of a relatively complex structure and large size. Inspired by [14], this paper aims to reduce the complexity of the radiating patch and overall antenna size by employing few and effective bandwidth enhancement techniques. The paper aims to achieve the antenna operation in mandatory channels of WBAN specified by IEEE 802.15.6. To our best knowledge, the proposed antenna is the one of the first microstrip-based antennas fully implemented using textiles with optimized use of miniaturization techniques, featuring a full rear ground plane designed for operation in the IEEE 802.15.6 WBAN mandatory channels. This paper is organized as follows. Section 2 presents a detailed design procedure for the proposed antenna. Section 3 presents the performance assessment in terms of reflection coefficients, bandwidth, gain, radiation patterns, fidelity, and specific absorption rate (SAR). The concluding remarks are provided in the final section.

2. Antenna Design and Textiles

The textile antenna substrate is made using a 3 mm-thick felt textile. Felt is chosen in this work based on its cost-effectiveness, ease of accessibility, and ease of fabrication in comparison to other textile materials such as Kevlar. The relative permittivity (ε_r) of felt is 1.45, and its loss tangent ($\tan\delta$) is 0.044. Meanwhile, ShieldIt Super from LessEMF Inc. [16] is 0.17 mm in thickness. Its conductivity is estimated to be 1.18×10^5 S/m [17]. The conductive textile is used to form the ground plane and radiating elements of the antenna. The final resulting structure is fabricated fully using textiles, except for the SMA connector which is integrated for evaluation purposes. The antenna design and simulations were carried out in CST Microwave Studio [18].

2.1. Antenna Design. A well-known procedure proposed in [19] is used to calculate the initial dimensions of the antenna theoretically. To maintain a full ground plane, the dimensions of the ground plane and substrate are kept equal and are optimized to achieve a compact size while maintaining a simple structure. As previously described, the antenna design with a full ground plane is adapted to preserve the antenna performance when operated closely to the human body. The substrate and full ground plane are optimized with a dimension of 39 mm × 42 mm. To achieve dual-band operation, two separate feedlines are optimized by combining them to radiate in LB (centered at 4 GHz) and HB (centered at 8 GHz); see Figure 1(a). Two feedlines consisting of a $11 \times 10\,\text{mm}^2$-shorter HB feed and a $20 \times 6\,\text{mm}^2$-longer LB feed are used to feed the two rectangular radiating structures. The corresponding performance of the reflection coefficients (S_{11}) from these feedlines are shown in Figure 2. It indicated a resonance centered at 3.5 GHz in LB and centered at 8.3 GHz in HB.

Radiator A, which is a combination of a simple square radiator and two L-shaped radiators, is then added to the HB feed on the left in Figure 1(a), prior to further optimization to obtain a wider operating bandwidth in HB. The two L-shaped radiators are combined with the square radiator to extend its operation in HB towards frequencies below 8 GHz, applying the concept of combined resonance. This square radiator radiates in HB between 9 and 10 GHz, whereas the L-shaped radiator radiates mainly at 8 GHz. The coupling between the square radiator and the folded L-shaped radiator also contributed to the bandwidth increase due to the added capacitance. The final combined antenna structure with the addition of radiator A is shown in Figure 1(b). A wide operating bandwidth of 2 GHz is achieved, operating between 7.7 GHz and 9.7 GHz in HB. Besides that, the combination with the narrow L-shaped radiator arms also introduced a single resonance with a bandwidth of 315 MHz at 6.5 GHz, as shown in Figure 2. This also resulted in a notch centered at 7 GHz with low impedance, contrary to about 50 Ω impedance observed throughout HB.

Upon the addition of radiator A to the feedline, another substructure, denoted as radiator B, is then integrated with the antenna. Its addition is aimed at achieving a wider bandwidth in HB by eliminating the notch band at 7 GHz, besides enabling operation in LB. To maintain simplicity, two L-shaped arms are used to form radiator B and optimized to achieve the two aims; see Figure 1(c). While optimizing radiator B, steps are taken to maintain the small size of the

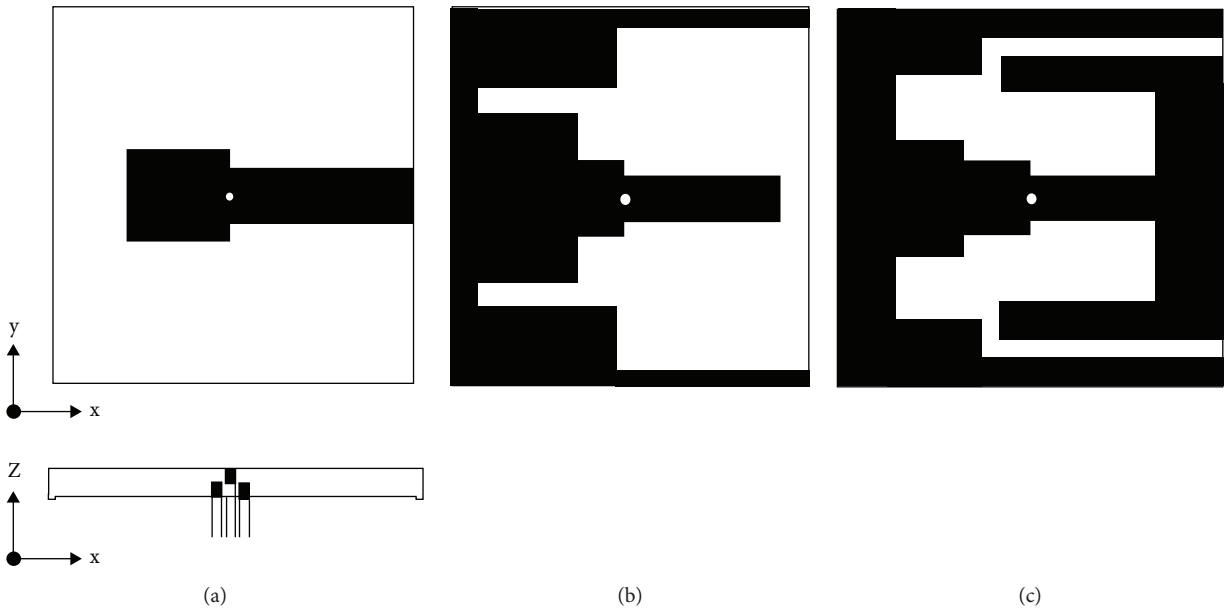

Figure 1: (a) Optimized feedlines and feedlines with the integration of (b) radiator A and (c) radiator B.

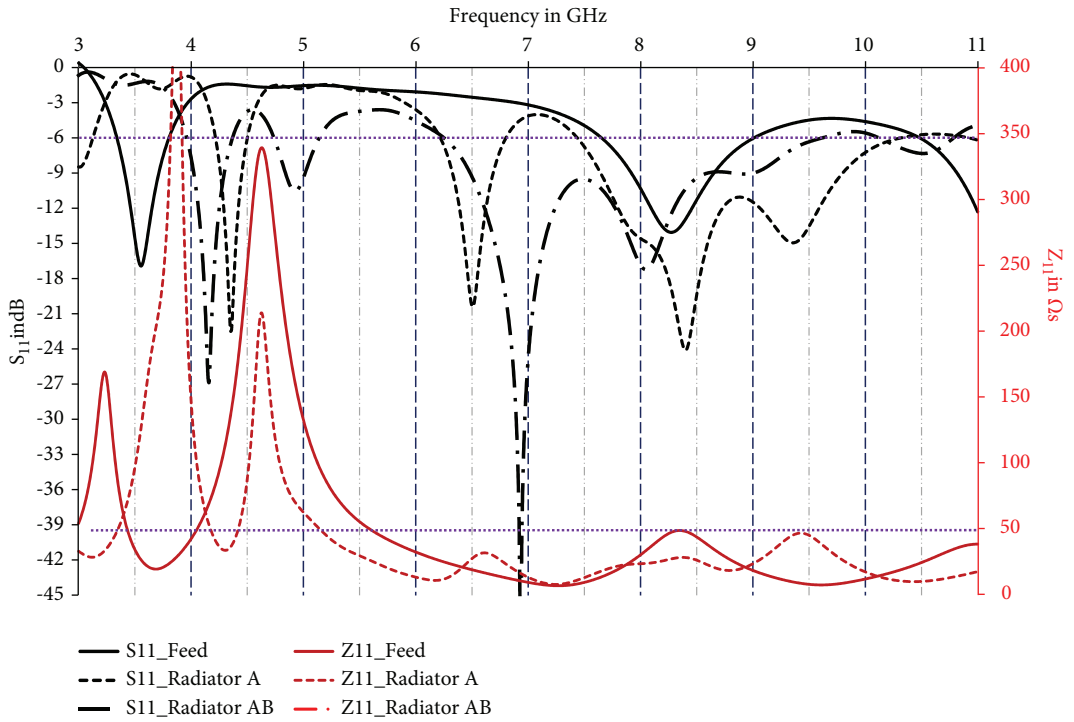

Figure 2: Reflection coefficients (S_{11}) and impedance (Z_{11}) with different modifications based on Figure 1 (feed, feed with radiator A, and feed with radiators A and B).

overall structure. With the addition of radiator B, the notch band at 7 GHz is eliminated, with a resonance at about 6.5 GHz; see Figure 2. Besides that, this modification also provided additional dual resonance at 4.2 GHz and 5 GHz in LB. However, the antenna exhibited a marginal operation at 5 GHz. To improve this, multiple impedance matching techniques are used in the next modification. The final topology that incorporates both radiators prior to the next optimization phase is shown in Figure 1(c).

Next, steps are introduced to improve impedance matching [20]. Specifically, a single step is introduced at the inner border of radiator B and two steps at the outer borders. The introduction of the steps increased the total bandwidth in LB by lowering the initial resonance at

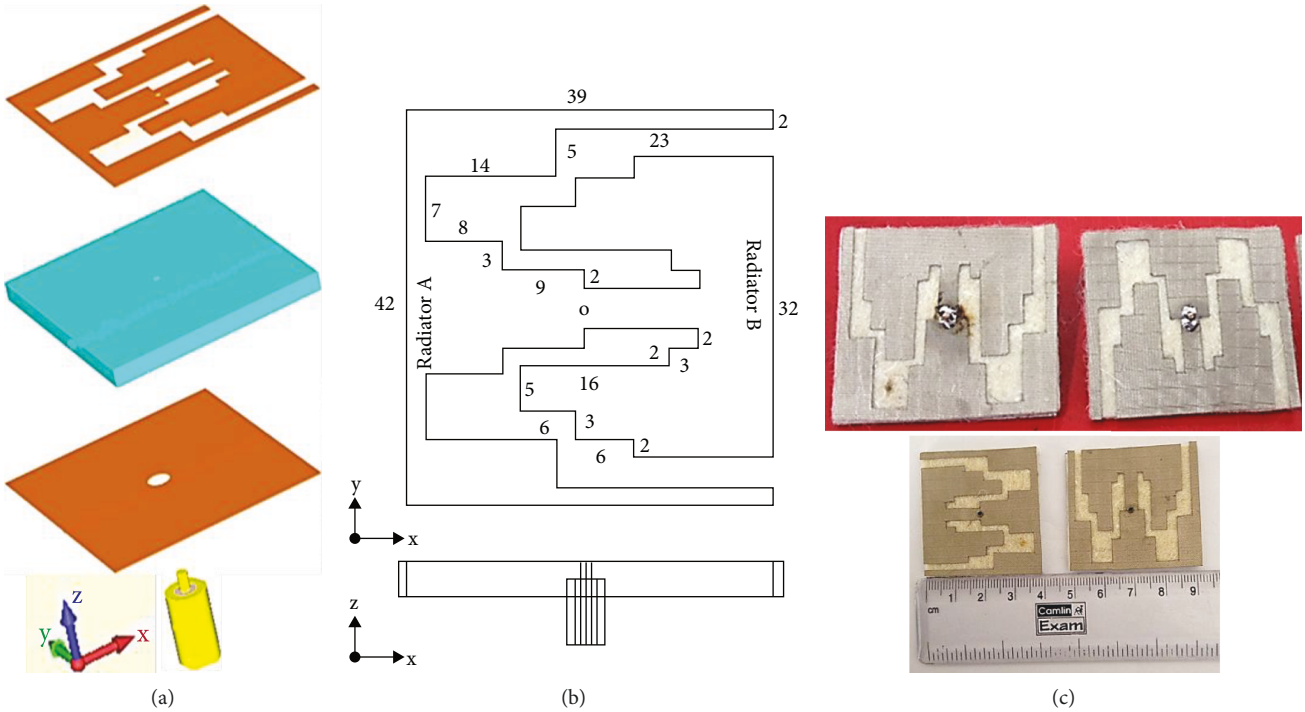

FIGURE 3: Design of the proposed antenna: (a) exploded view; (b) dimensions (in mm); (c) fabricated prototype (top) and fabricated prototype prior to soldering feed (bottom).

5 GHz. The steps introduced on the outer borders also improved the bandwidth in HB by enhancing parasitic coupling from radiator A.

2.2. Final Antenna Topology. The final antenna topology is a three-layered structure symmetrical at the x-axis as shown in Figure 3(a). The middle layer felt substrate is sandwiched between two conductive ShieldIt layers. The top layer is the radiating layer (with radiators A and B), and the full ground plane layer is at the bottom. The overall antenna size is 42 $\times$ 39 mm^2 with a total thickness of 3.34 mm as shown in Figure 3(b). The feedlines to the two radiators (A and B) are fed using a coaxial cable from its center. To achieve a wide bandwidth in HB with a dual property, two bandwidth enhancement techniques are combined and used. They are (1) the multiresonance technique with two radiators [21] and (2) the parasitic coupling technique between two radiators [22]. Furthermore, the individual line widths that feed the respective radiators are optimized to achieve a notching property between LB and HB. The proposed antenna design employs the minimum use of bandwidth enhancement techniques to reduce the radiator complexity and to minimize radiation pattern distortions. Radiator A uses a resonance overlapping technique between a simple square patch and two L-shaped sections to achieve a wide bandwidth in HB. Radiator B consists of a simple L-shaped radiator. Steps are introduced onto their feedlines to improve impedance matching. The nonuniform gap that provides parasitic coupling between the borders of radiators A and B is optimized with the smallest gap of 2 mm. This is maintained in order to reduce fabrication errors, as the antenna is fabricated using simple manual cutting tools. The fabricated prototypes are shown in Figure 3(c). The prototypes were fabricated manually using simple cutting tools [10]. Firstly, ShieldIt and felt textiles are dimensioned into their required shapes and sizes using manual tools such as a knife, scissors, and scale. Then, an ironing process is applied onto the ShieldIt textile when placed on the felt textile to secure the textile onto the substrate. A hole is made through the substrate and ground plane before the placement of a 50 Ω SMA connector.

3. Simulation and Measurement Results

All simulations were performed in CST Microwave Studio software using a transient solver. During the design stage, initial simulations are performed with low mesh and low accuracy to achieve efficient computation as mentioned in [20]. This is performed prior to detailed simulations with high accuracies of up to -40 dB and with high mesh settings. Besides the evaluations in free space (FS), the antenna is also evaluated on body (OB) to characterize its robustness in terms of performance. OB simulations were performed by placing an antenna in close proximity to a simplified two-third muscle equivalent homogenous body model [4], sized at $66 \times 64 \times 44$ mm^3. Its relative permittivity is 50.8 and its conductivity is 3 S/m between 3 and 11 GHz. The proposed antenna is located at the center above this tissue model with an air gap of 10 mm as shown in Figure 4(a). This air gap is a realistic approximation of the actual placement of a wearable antenna on the human body with clothing [6, 17]. Furthermore, to validate the on-body simulation, a detailed human body voxel model (as shown in Figure 4(b)) with a resolution of $2 \times 2 \times 2$ mm^3 is used in CST by placing the proposed antenna at a distance of 10 mm from the upper

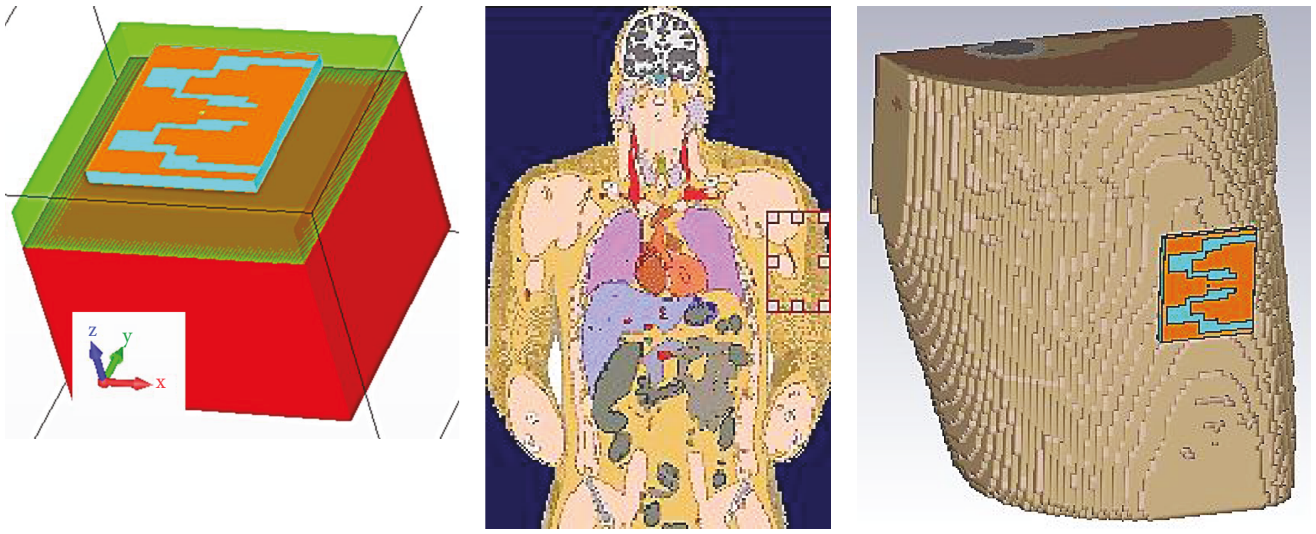

(a) (b) (c)

Figure 4: On-body simulation setup using (a) a simplified homogenous body model and (b) a human body voxel model. (c) Placement on the upper-arm section of the model.

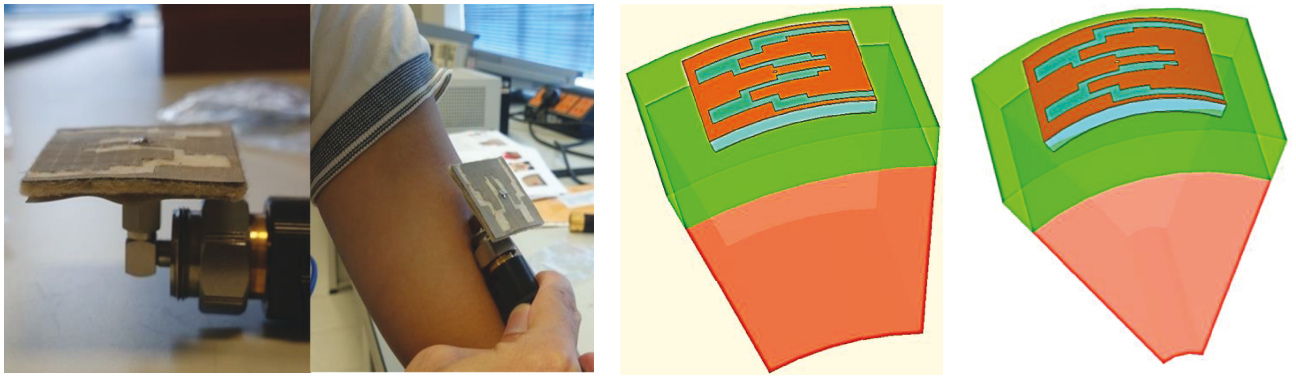

(a) (b) (c)

Figure 5: On-body simulation setup for (a) FS and OB experimental setup at (b) 30° bending and (c) 60° bending.

arm section of the model (see Figure 4(c)). The proposed antenna is also assessed under two bent conditions on body (simplified homogenous body model), bend angles of 30° and 60° as shown in Figures 5(a) and 5(b). The bend tool from CST Microwave Studio is used to bend the antenna and body model (including the airgap) cylindrically with the intended angles defined towards both directions from the center of the structure. Two antenna parameters, S_{11} and realized gain, are evaluated under these bent conditions prior to their performance analysis.

Three prototypes, Prototype 1 (P1), Prototype 2 (P2), and Prototype 3 (P3), were fabricated. The FS and OB experimental setup is shown in Figure 5(a). For OB S_{11} measurements, the prototypes were placed on the arm at a distance of 10 mm to validate the simulation results obtained when the proposed antenna is placed on both the simplified equivalent homogenous model and the voxel model.

3.1. Reflection Coefficient (S_{11}). The proposed all-textile antenna fulfills several operating bands within the UWB-WBAN application as specified by the IEEE 802.15.4 standard. In the UWB-LB, the proposed antenna successfully operated from 3.65 GHz to 4.30 GHz with a total operable bandwidth of 650 MHz in free space based on the -6 dB limits; see Figure 6. It successfully achieves its operation in

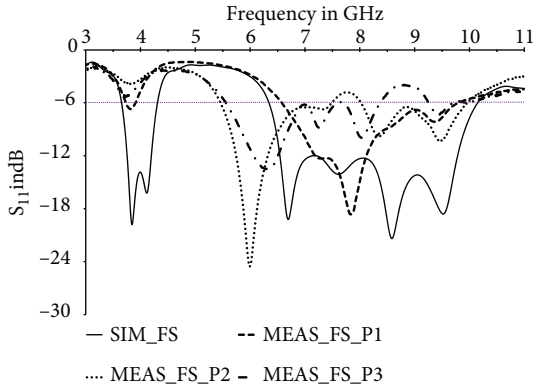

Figure 6: Simulated and measured S_{11} of the proposed antenna in FS.

Table 1: Comparison between the operation of the proposed antenna in FS (measured with $S_{11} < -6$ dB) with the 802.15.6 standard channels [5].

Band group	Channel no.	Center freq. (MHz)	Channel BW (MHz)	FS simulated BW (MHz)	FS measured BW (P1)	FS measured BW (P2)	FS measured BW (P3)
Low band (LB)	0	3494.4 (O)	3244.8–3744.0	3655.9–3744.0	—	—	—
	1	3993.6 (M)	3744.0–4243.2	3744.0–4243.2	3700–3810	—	—
	2	4492.8 (O)	4243.2–4742.4	4243.2–4303.9	—	—	—
High band (HB)	3	6489.6 (O)	6240.0–6739.2	6343.9–6739.2	6610–6739.2	6240.0–6739.2	6240.0–6739.2
	4	6988.8 (O)	6739.2–7238.4	6739.2–7238.4	6739.2–7238.4	6739.2–7238.4	6739.2–7238.4
	5	7488.0 (O)	7238.4–7737.6	7238.4–7737.6	7238.4–7737.6	7238.4–7560.0	7238.4–7737.6
	6	7987.2 (M)	7737.6–8236.8	7737.6–8236.8	7737.6–8236.8	7990.0–8236.8	7737.6–8236.8
	7	8486.4 (O)	8236.8–8736.0	8236.8–8736.0	8236.8–8736.0	8236.8–8736.0	8236.8–8390.0
	8	8985.6 (O)	8736.0–9235.2	8736.0–9235.2	8736.0–9235.2	8736.0–9235.2	—
	9	9484.8 (O)	9235.2–9734.4	9235.2–9734.4	9235.2–9734.4	9235.2–9734.4	9240.0–9734.4
	10	9984.0 (O)	9734.4–10233.6	9734.4–1014.4	9734.4–9800.0	9734.4–9990.0	9734.4–9990.0

the mandatory Channel (M) 1 (of UWB-LB) as shown in Table 1. Meanwhile, the antenna operated partially in the optional (O) Channels 0 and 2, with the operating bands of 88.1 MHz and 60.7 MHz, respectively. In HB, a wide bandwidth of 3.8 GHz is achieved in FS, operating from 6.3 GHz to 10.1 GHz; see Figure 6. This indicates the coverage from Channels 4 to 9 as shown in Table 1, including the mandatory Channel 6 centered at 7.897 GHz. Partial operation is achieved in Channels 3 and 10, with an operating bandwidth of 396 MHz and 66 MHz, respectively. The FS S_{11} measurement results of three fabricated prototypes are illustrated in Figure 6 indicating a satisfactory agreement with simulation results. The measured S_{11} of Prototype 1 (P1) exhibited a partial operation in mandatory Channel 1 in LB with 110 MHz of bandwidth. A major detuning is observed in LB with no operation in both Channels 0 and 2. This is caused by the variation of its thickness due to its flexibility, one of the major causes of antenna detuning when evaluated in free space [23]. Meanwhile in HB, the operation in all Channels from 3 to 10 is achieved with partial operation in Channels 3 and 10, as shown in Table 1. Partial operation with the bandwidths of 129 MHz and 66 MHz is achieved for Channels 3 and 10, respectively. Between simulated and measured S_{11}, detuning is observed in LB and a shift of operation to lower frequency by 800 MHz is observed for Prototype 2 (P2) and Prototype 3 (P3). Prototype 2 achieved its operation in all channels of HB with partial operation in Channels 5 and 6, with the operational bandwidths of 322 MHz and 247 MHz, respectively. Prototype 3 operated in all HB channels except in the optional Channel 8. Details of each prototype's operation are summarized in Table 1.

The OB response in LB exhibited a slight degradation in the operating bandwidth, as shown in Figure 7. The proposed antenna maintained its operability in the mandatory Channel 1 with a bandwidth of around 496 MHz (operating from 3.8 to 4.3 GHz). The OB S_{11} response in HB agrees well with the response in FS, with a shift of its operating region by 272 MHz towards the higher frequencies. Compared to measurements in FS, although the partial operating bandwidth in Channel 3 is reduced by 5 MHz, it successfully achieved its full operation in Channel 10 when placed on body. On the other hand, the on-body S_{11} response with the human body voxel model is also shown in Figure 7. The on-body S_{11} response with the voxel model agrees very well with the on-body S_{11} response when placed near the simplified body model, with minor degradations observed, especially at 4 GHz and 8 GHz. The OB measurement of S_{11} was performed for prototypes 2 and 3. Compared to OB simulation results, the measurement results exhibited a major detuning in LB as shown in Figure 7. In HB, both measured S_{11} exhibited a shift of operation to lower frequency by about 1 GHz. Despite observing this behavior for both prototypes, they operated in all HB channels. Prototype P2 achieved its full operation in Channels 3, 4, 7, and 8, and it partially operated in Channels 5, 6, and 10 with the operating bandwidths of 332 MHz, 237 MHz, and 218 MHz, respectively. Prototype P3 achieved its full operation in Channels 3, 4, 5, and 9, including the mandatory Channel 6. It partially operated in Channels 7, 8, and 10 with the operating bandwidths of 213 MHz, 51 MHz, and 436 MHz, respectively. The detailed comparison of the OB simulation and measurements is presented in Table 2.

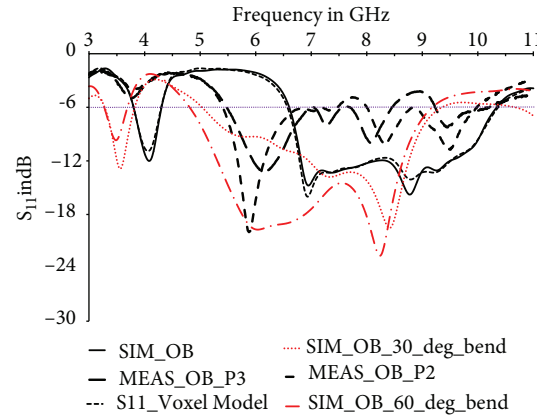

Figure 7: Simulated and measured S_{11} of the proposed antenna on body.

Table 2: Comparison between the operation of the proposed antenna in OB (measured with S_{11} < -6 dB) with the 802.15.6 standard channels.

Band group	Channel no.	Center freq. (MHz)	Channel BW (MHz)	OB simulated BW (MHz)	OB measured BW (P2)	OB measured BW (P3)	OB simulated 30° bend	OB simulated 60° bend
Low band (LB)	0	3494.4 (O)	3244.8–3744.0	—	—	—	3343.2-3744.0	3286.9-3697.6
	1	3993.6 (M)	3744.0–4243.2	3807.9–4243.2	—	—	3744.0-3827.0	—
	2	4492.8 (O)	4243.2–4742.4	4243.2-4303.9	—	—	—	—
High band (HB)	3	6489.6 (O)	6240.0–6739.2	6615.9-6739.2	6240.0–6739.2	6240.0–6739.2	6240.0–6739.2	6240.0–6739.2
	4	6988.8 (O)	6739.2–7238.4	6739.2–7238.4	6739.2–7238.4	6739.2–7238.4	6739.2–7238.4	6739.2–7238.4
	5	7488.0 (O)	7238.4–7737.6	7238.4–7737.6	7238.4–7570.0	7238.4–7737.6	7238.4–7737.6	7238.4–7737.6
	6	7987.2 (M)	7737.6–8236.8	7737.6–8236.8	8000.0–8236.8	7737.6–8236.8	7737.6–8236.8	7737.6–8236.8
	7	8486.4 (O)	8236.8–8736.0	8236.8–8736.0	8236.8–8736.0	8236.8–8450.0	8236.8–8736.0	8236.8–8736.0
	8	8985.6 (O)	8736.0–9235.2	8736.0–9235.2	8736.0–9235.2	9184.0–9235.2	8736.0–9235.2	8736.0–9182.8
	9	9484.8 (O)	9235.2–9734.4	9235.2–9734.4	9235.2–9734.4	9235.2–9734.4	9235.2–9323.5	—
	10	9984.0 (O)	9734.4–10233.6	9734.4–10233.6	9734.4–9951.9	9734.4–10170.0	—	—

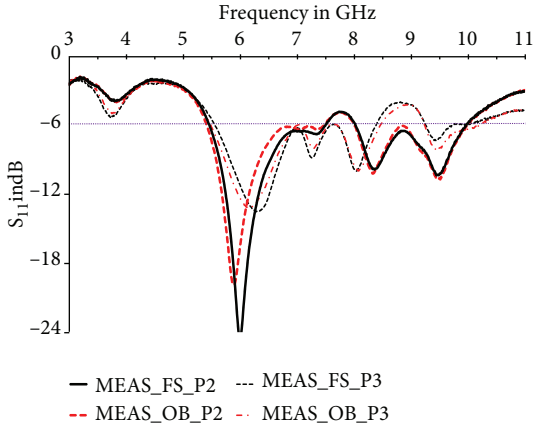

Figure 8: Comparison between measured S_{11} in FS and OB.

The proposed antenna is further evaluated under bent conditions in simulations using the simplified body model at 30° and 60° bends. It successfully preserved its operation in the mandatory Channel 1 when bent at 30°, along with partial operation in Channel 0 as presented in Table 2. In HB, the proposed antenna successfully operated from Channels 3 to 9, including the mandatory Channel 6 under the 30° bent condition. When bent at 60°, the proposed antenna also successfully preserved its operation from Channels 3 to 8, including the mandatory Channel 6 in HB as shown in Figure 7. However, its operation in the LB mandatory channel is poor. Meanwhile, a partial operation in Channel 0 of LB and Channel 8 of HB is observed, with the operating bandwidths of 411 MHz and 386 MHz, respectively. The measured OB S_{11} results are in good agreement with the measured S_{11} result in FS, as illustrated in Figure 8. This indicates the ability of the proposed prototype in preserving the performance when placed on body.

3.2. Radiation Performance. The radiation patterns of the antenna are then assessed in the *yz* and *xz* planes. The radiation in the *xz* plane is measured by varying θ at $\varphi = 0°$ cut. Meanwhile the *yz* plane patterns are evaluated by varying θ at $\varphi = 90°$ cut. Both cuts are evaluated at the center operating frequency of each channel, in both FS and OB. In the mandatory LB channel, the pattern is evaluated at 4 GHz, which is the center frequency of Channel 1. Meanwhile, in HB, radiation patterns were assessed at 7, 7.5, 8, 8.5, and 9 GHz, which are the center frequencies of Channels 4, 5, 6, 7, and 8. Radiation patterns in FS and OB are illustrated in Figure 9 at both the *xz* and *yz* planes. The radiation patterns for Channel 1 shown in Figure 9(a) are symmetrical and quasiomnidirectional in the *yz* plane due to the symmetrical antenna topology at the *y*-axis. The antenna featured a broadside radiation pattern with a half-power beamwidth (HPBW) of 66.7°. An asymmetrical radiation pattern with reduced omnidirectivity is observed in the *xz* plane. The characteristics of the radiation patterns are tabulated in Table 3. The OB radiation patterns in both the *xz* and *yz* planes exhibit sharp nulls at $\theta = 180°$, with several smaller nulls in the back radiation from $\theta = 90°$ to 270° in both planes. In the *yz* plane, the proposed antenna preserves its broadside radiation, maintaining almost the same main lobe magnitude and the angular width. Meanwhile, in the *xz* plane, the angular width is reduced from 71.8° to 62.3°.

The FS and OB radiation patterns in HB are shown in Figures 9(b)–9(f) for both *yz* and *xz* planes. The proposed antenna generally exhibited omnidirectional and nonuniform radiation patterns in free space. Several dominant beams are also observed in the *xz* plane. As shown in Figures 9(b)–9(d), the antenna exhibits more radiation directed towards the half section (from $\theta = 180°$ to 360°) in the *xz* plane at 7, 7.5, and 8 GHz. The patterns at these frequencies exhibited similar characteristics, with the diminishing of the sharp null at $\theta = 180°$ with an increase in the frequency. Meanwhile, the OB radiation at these frequencies exhibited its ability to preserve the pattern on broadside when placed on the homogenous body model. The broadside pattern is similar to the FS pattern, with major null points at the same θ angles and with similar angular width. A minor change in magnitude of the null points is observed, with smaller nulls at the back radiation. The nonuniform radiation with ripples in its back radiation observed is mainly due to the coupling with the homogenous body model, indicating a reduction of the back radiation at the three

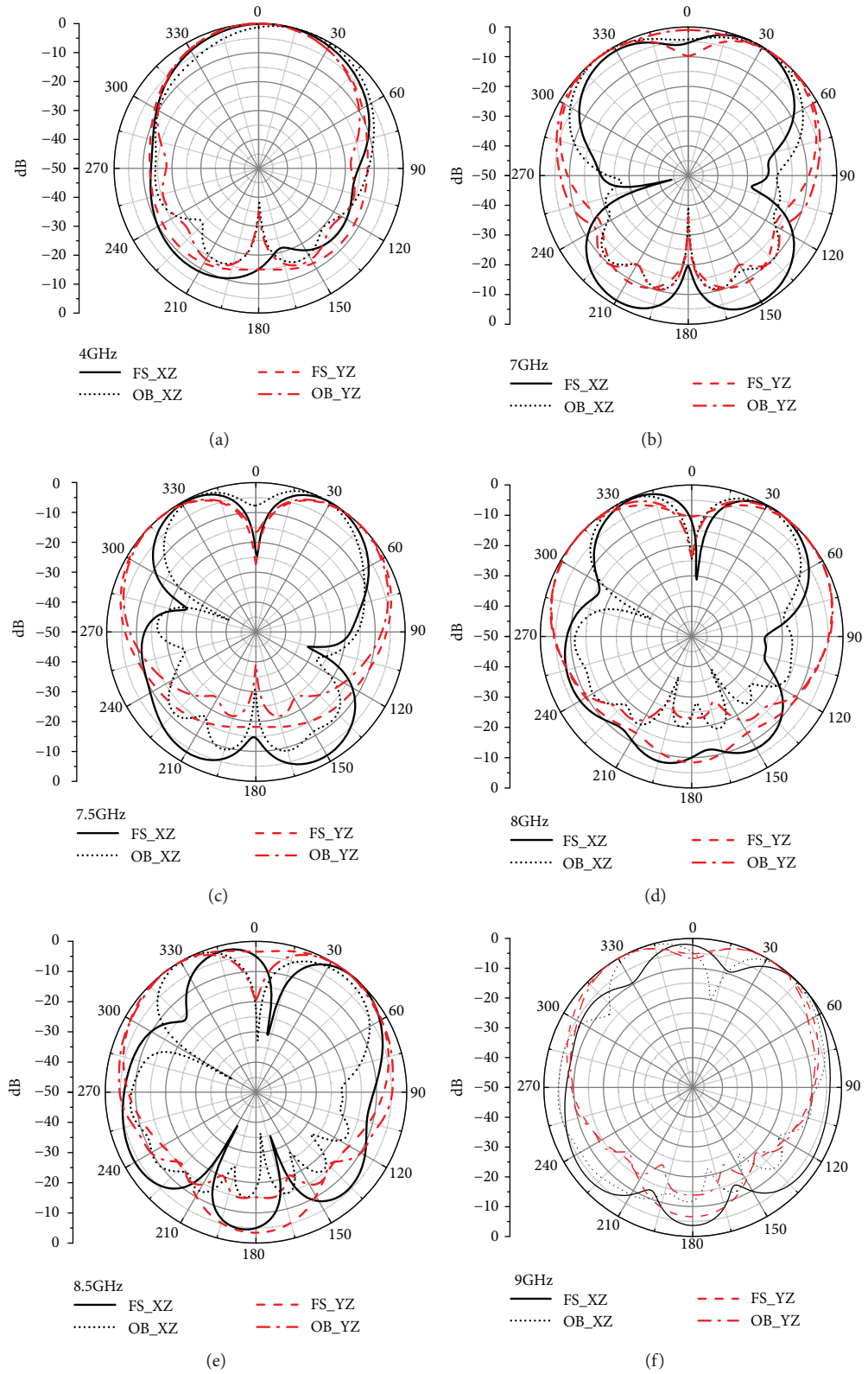

Figure 9: Free space and on-body radiation patterns at (a) 4 GHz, (b) 7 GHz, (c) 7.5 GHz, (d) 8 GHz, (e) 8.5 GHz, and (d) 9 GHz.

frequencies. Meanwhile, at 8.5 and 9 GHz, the shift in the null locations is exhibited in the OB patterns. The radiation tends to be directed towards the right half in the *xz* plane, as shown in Figures 9(e) and 9(f). In the *xz* plane at 8.5 GHz, a uniform omnidirectional pattern is observed in FS with small nulls. All FS patterns in the high band excluding the radiation at 8 GHz displayed a high side lobe level ranging between -1 and -2.3 dB in the *xz* plane; see Table 3. Meanwhile, at

Table 3: Comparison of radiation patterns parameters in both FS and OB.

Band	Centre frequency (GHz)	Plane	Main lobe magnitude (dBi)		Half-power beamwidth (HPBW)		Side lobe level (dB)	
			FS	OB	FS	OB	FS	OB
Low band	4	*xz*	7.5	8.9	71.8°	62.3°	-8.7	-13.9
		yz	7.4	7.6	66.7°	64.9°	-11.5	13.6
High band	7	*xz*	0.4	3.9	38.4°	43.7°	-1.0	-9.7
		yz	4.8	0.8	47.8°	38.3°	-9.0	-9.7
	7.5	*xz*	-0.3	-4.1	35.1°	32.9°	-2.3	-8.8
		yz	3.4	4.8	53.6°	49.6°	—	-20.7
	8	*xz*	3.6	3.5	34.5°	29.9°	-7.1	-11.3
		yz	2.0	2.9	56.7°	63.2°	-8.5	-16.2
	8.5	*xz*	5.9	5.7	36.1°	28.9°	-1.9	-1.9
		yz	4.3	2.9	60.1°	56°	-3.4	-13.3
	9	*xz*	3.8	4.7	46.7°	40.9°	-1.9	-4.6
		yz	6.7	6.7	47.5°	39.9°	-6.6	-13.7

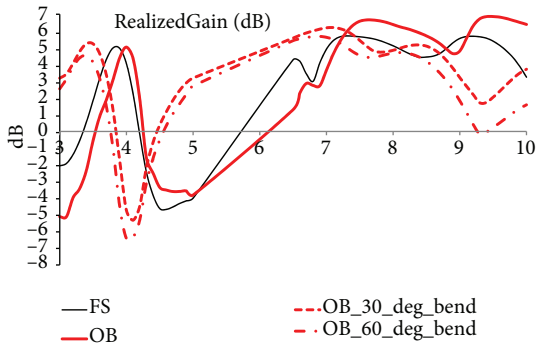

Figure 10: Simulated realized gain in FS, OB, and under bend condition.

8 GHz, the pattern exhibited a beam width of 34.5° with a reduced lower side lobe of -7.1 dB.

In the *yz* plane, the evaluated radiation pattern in FS and OB exhibited a directional pattern with maximum broadside radiation at the centre frequency of the individual channels in HB. The radiation of the proposed antenna exhibited robustness with consistent broadside radiations in the *yz* plane throughout the high band in both FS and OB. Relative to the *xz* plane, the better consistency of the radiation is evident in the *yz* plane. At 8 and 8.5 GHz, sharp nulls are observed at $\theta = 0°$. The antenna also exhibited a dual beam property with a broadside angle of $\theta = \pm 30°$ at 7.5, 8, and 8.5 GHz in the *yz* plane. This characteristic is observed to diminish with an increase in channel frequency. When placed on body, such property tend to become more visible at 8 GHz and 8.5 GHz with deeper nulls. The evaluated OB pattern throughout the high band exhibits reduced low back radiation, with the appearance of more ripples as the frequency increases. Details of the properties of the radiation patterns in the high band are summarized in Table 3.

3.3. Evaluation of Realized Gain and Fidelity. The simulated realized gains of the proposed antenna in FS, OB, and under OB bend conditions are shown in Figure 10 and summarized in Table 4. They are evaluated at the center frequency of each operating WBAN-UWB channel (Channels 1, 4, 5, 6, 7, 8, and 9) in FS, OB, and under bent conditions (30° and 60° of bending). The proposed antenna exhibited high antenna gains in FS and OB for both LB and HB. A similar gain pattern is exhibited when placed on a homogenous body model with a shift towards higher frequency by 200 MHz in LB. In Channel 1, compared to FS, the OB realized gain increased from 4.16 dB to 4.42 dB. The proposed antenna exhibited high-realized gains in FS throughout the high band. It offered a gain of 5 dB at the center frequency of Channels 4 and 6. Meanwhile, a realized gain of 6 dB is observed in Channels 5, 8, and 9. OB evaluations further increased the gain in the high band by an average of 1 dB except in Channels 4 and 8. The gain in Channel 4 is decreased by about 2 dB from 4.8 dB to 2.7 dB. On the contrary, realized gains are negative in value throughout the notch band. Meanwhile, under both 30° and 60° bent conditions, the proposed antenna fails to preserve its performance in the mandatory Channel 1, producing negative gains. However, the antenna maintained high gains in HB, throughout Channels 3 to 9. High gains of between 4 and 6 dB are featured in Channels 3 to 7 when evaluated with 30° and 60° bends.

The FS simulation of the fidelity factor was performed by placing farfield probes at a distance of 10 cm from the proposed antenna. Fidelity is evaluated by determining the peak of the cross correlation between the port and the probe signal [24]. The probes are placed by varying θ in a fixed step of 20° in the *xz* plane ($\varphi = 0°$) and *yz* plane ($\varphi = 90°$). The simulation setup is shown in Figure 11. The default Gaussian excitation port signal was used to compute the cross correlation. The computed fidelity shown in Figure 12 indicated a maximum fidelity of 87% at $\theta = 140°$ in the *xz* plane. Meanwhile, in the *yz* plane, the maximum fidelity factor is 71.2%

Table 4: Realized gain at the centre frequency of each WBAN-UWB channel.

Group band	Channel no.	Centre frequency (GHz)	Realized gain in free space (dB)	Realized gain on body (dB)	30° bent realized gain (OB) (dB)	60° bent realized gain (OB) (dB)
Low band	1	3.99	4.16	4.42	-1.72	-4.49
	3	6.49	4.29	1.30	5.44	5.59
	4	6.99	4.89	2.74	6.12	5.69
	5	7.49	5.67	6.6	5.45	4.56
High band	6	7.99	5.14	6.4	4.78	4.61
	7	8.49	4.46	5.73	5.11	4.21
	8	8.99	5.55	4.82	3.77	2.48
	9	9.49	5.42	6.88	2.05	0.23

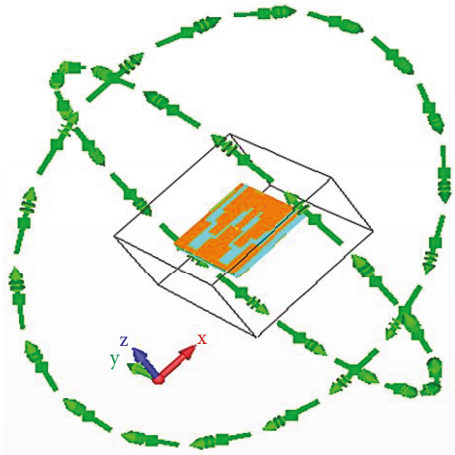

Figure 11: Fidelity simulation setup for the *xz* and *yz* planes.

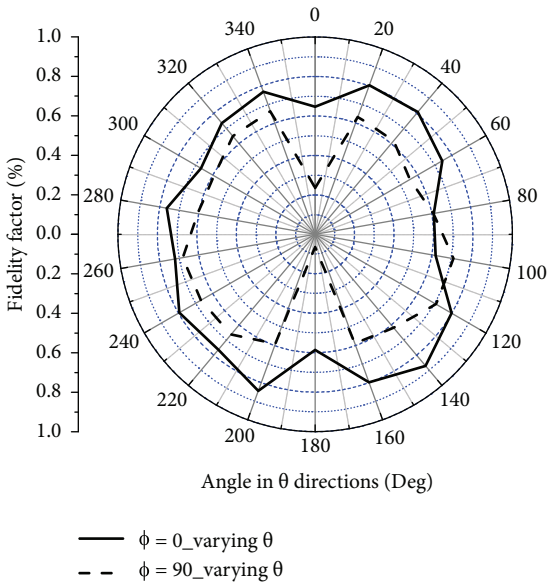

Figure 12: Fidelity factor in the *xz* and *yz* planes.

at $\theta = 100^{\circ}$. The average fidelity in the *xz* plane is 73.6%, which is acceptable.

3.4. SAR and Comparison Evaluation. Finally, the specific absorption rate (SAR) is evaluated using a detailed human body voxel model in CST. The SAR evaluations were performed at two frequency points, 4 GHz and 8 GHz, with an input power of 0.5 W (rms) [25]. The calculated SAR at these frequencies are well under the Federal Communications Commission- (FCC-) regulated limit of 1.6 W/kg averaged over 1 g of tissue [26], with values of 0.335 and 0.491 W/kg, respectively; see Figure 13.

To highlight the uniqueness of the proposed antenna, it is compared with existing UWB antennas designed for WBAN applications. Existing UWB antennas with different topologies are selected and compared in terms of operating bandwidth, notching property, overall size, and ground plane type, as listed in Table 5. It is shown that the most popular method to achieve UWB band with minimized antenna size is by using the CPW topology with either partial or slotted ground planes. However, the coupling introduced by the use of such techniques has shown to degrade the antenna performance when operated on the human body [14]. In addition, the presence of back radiation reduces the attractiveness of such antennas for employment in WBAN applications. The comparison against existing UWB antennas with a full ground plane also indicated the achievement of FCC-compliant UWB characteristics with larger sizes as compared to the proposed antenna. Besides that, introducing the notching property in such UWB antennas for IEEE WBAN compliance will result in added complexity and size while simultaneously trying to implement a full ground plane. On the contrary, the proposed antenna provides a compact topology with notching property and low complexity to enable operation in the UWB bands specified by the IEEE WBAN standard.

4. Conclusion

A miniaturized all-textile antenna with a simple antenna topology is proposed for its application in UWB-WBAN specified by the IEEE 802.15.4 standard. It has an overall size of $39 \times 42 \times 3.14\,\text{mm}^3$ and incorporates two broadbanding techniques to maintain a simple radiator topology. The two bandwidth enhancement techniques, multiresonance overlapping and parasitic coupling, provided successful operation in both LB and HB channels of WBAN. The proposed antenna successfully achieved its operation in all channels of LB and HB with notching properties from 4.6 to 6.5 GHz. The proposed antenna, when evaluated on body,

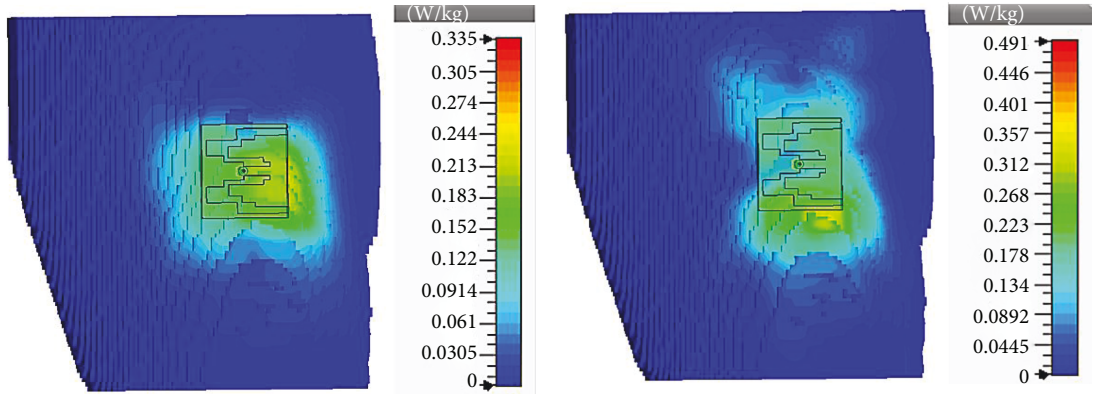

(a) (b)

Figure 13: SAR evaluation at (a) 4 GHz and (b) 8 GHz.

Table 5: Comparison of the proposed antenna with available UWB antennas in literature.

Ref no.	Antenna topology	Operating frequency (GHz)	Targeted operating UWB band	Notching property	Overall size in λ (lowest operating frequency)	Ground plane (GP)	Bandwidth enhancement techniques
[14]	Microstrip	3.6–10.3	FCC	None	1.16λ	Full GP	Multiresonance, slots and parasitic element
[27]	Printed microstrip	4–9.5	FCC	None	1.13λ	Full GP	Multiresonance, slots and parasitic element
[28]	Three-layered antenna	3.18–11	FCC	None	0.85λ	Full GP	Multi- (three) stacking layers
[29]	Antenna with partial ground plane	2.7–19.5	FCC	None	0.36λ	Partial and slotted GP	Partial and slotted ground plane, slots
[30]	CPW fed—tapered	3–5.1, 5.35–12	FCC with single notch	Single notch to reject 5 GHz WLAN band	0.26λ	NA	Vivadi structure
Proposed antenna	Microstrip	3.9–4.2, 6.5–9.9	IEEE WBAN-UWB	Single notch to reject 5 GHz WLAN band	0.55λ	Full GP	Multiresonance and active coupling

operated in the mandatory Channel 1 and optional Channel 2 in LB. Meanwhile, in HB, the proposed antenna successfully operated in all channels (from Channels 3 to 10), including the mandatory Channel 6. The evaluation results of the S_{11} response and realized gain of the proposed antenna under bend angles of 30° and 60° by placing it on a simplified body model are presented. The proposed antenna exhibited an ability to preserve its performance in HB under bending conditions. The SAR evaluation of the proposed antenna is also presented, exhibiting a satisfactory fidelity factor in the *xz* plane with an average of 73.6% in free space fidelity. On the other hand, its SAR level of 0.491 W/kg fulfills the absorption requirement specified by FCC.

Data Availability

The simulation and experimental data used to support the findings of this study are available from the corresponding author (purna.cst@rub.edu.bt) upon request. The observational data comparing the proposed antenna against other available antennas are included within the article.

Conflicts of Interest

The authors declare that there are no conflicts of interest.

Acknowledgments

The authors acknowledge the technical support of Dr. Herwansyah Lago from Universiti Malaysia Sabah. His PhD in UniMAP was supported by the Malaysia Ministry of Education via the MyBrain15 Programme. This work was partly supported by the Annual University Research Grant 2014 (AURG-2014) of the Royal University of Bhutan, Universiti Teknikal Malaysia Melaka's Research Grant (Grant no: JURNAL/2018/F-KEKK/-Q00001), and the Fundamental Research Grant Scheme (FRGS) from the Malaysia Ministry of Higher Education (Grant no: FRGS/1/2015/ICT05/UNIMAP/02/2).

References

[1] Federal Communications Commission, *FCC Report and Order for Part 15: Acceptance of Ultra-Wideband (UWB) Systems from 3.1–10.6 GHz*, Federal Communications Commission (FCC), 2002.

[2] N. Chahat, M. Zhadobov, R. Sauleau, and K. Ito, "A compact UWB antenna for on-body applications," *IEEE Transactions on Antennas and Propagation*, vol. 59, no. 4, pp. 1123–1131, 2011.

[3] A. Alomainy, Y. Hao, C. G. Parini, and P. S. Hall, "Comparison between two different antennas for UWB on-body propagation measurements," *IEEE Antennas and Wireless Propagation Letters*, vol. 4, pp. 31–34, 2005.

[4] P. J. Soh, S. J. Boyes, G. A. E. Vandenbosch, Y. Huang, and S. L. Ooi, "On-body characterization of dual-band all-textile PIFA," *Progress In Electromagnetics Research*, vol. 129, pp. 517–539, 2012.

[5] "IEEE standard for local and metropolitan area networks—part 15.6: wireless body area networks," 2012, IEEE Standard 802.15.6TM.

[6] D. Ghosh and P. K. Sahu, "UWB in healthcare," in *2016 International Conference on Electromagnetics in Advanced Applications (ICEAA)*, pp. 679–682, Cairns, Australia, 2016.

[7] G. Adamiuk, T. Zwick, and W. Wiesbeck, "UWB antennas for communication systems," *Proceedings of the IEEE*, vol. 100, no. 7, pp. 2308–2321, 2012.

[8] Nitika, V. Singh, G. S. Brar et al., "High gain multifaceted novel UWB flexible microstrip patch antennas for indoor location and tracking equipment applications," in *2016 Progress in Electromagnetic Research Symposium (PIERS)*, pp. 1105–1109, Shanghai, China, 2016.

[9] R. Bharadwaj, S. Swaisaenyakorn, C. Parini, J. Batchelor, and A. Alomainy, "Motion tracking of a human subject in healthcare applications using compact ultra wideband antennas," in *Proceedings of the 4th International Conference on Wireless Mobile Communication and Healthcare—"Transforming Healthcare through Innovations in Mobile and Wireless Technologies"*, pp. 199–202, Athens, Greece, 2014.

[10] P. J. Soh, G. A. E. Vandenbosch, S. L. Ooi, and M. R. N. Husna, "Wearable dual-band Sierpinski fractal PIFA using conductive fabric," *Electronics Letters*, vol. 47, no. 6, pp. 365–367, 2011.

[11] P. B. Samal, P. J. Soh, H. Xu, and G. A. E. Vandenbosch, "Microstrip-based all-textile unidirectional UWB antenna with full ground plane," in *The 8th European Conference on Antennas and Propagation (EuCAP 2014)*, pp. 1408–1412, The Hague, Netherlands, 2014.

[12] B. Sanz-Izquierdo, J. C. Batchelor, and M. I. Sobhy, "Compact UWB wearable antenna," in *2007 Loughborough Antennas and Propagation Conference*, pp. 121–124, Loughborough, UK, 2007.

[13] K. Baskaran, C. P. Lee, C. K. Chakrabarty, and A. Compact Microstrip, "Antenna for ultra-wideband applications," *European Journal of Scientific Research*, vol. 67, no. 1, pp. 45–51, 2011.

[14] P. B. Samal, P. J. Soh, and G. A. E. Vandenbosch, "UWB all-textile antenna with full ground plane for off-body WBAN communications," *IEEE Transactions on Antennas and Propagation*, vol. 62, no. 1, pp. 102–108, 2014.

[15] P. J. Soh, G. Vandenbosch, F. H. Wee, A. van den Bosch, M. Martinez-Vazquez, and D. Schreurs, "Specific absorption rate (SAR) evaluation of textile antennas," *IEEE Antennas and Propagation Magazine*, vol. 57, no. 2, pp. 229–240, 2015.

[16] P. J. Soh, B. van den Bergh, H. Xu et al., "A smart wearable textile array system for biomedical telemetry applications," *IEEE Transactions on Microwave Theory and Techniques*, vol. 61, no. 5, pp. 2253–2261, 2013.

[17] P. J. Soh, G. A. E. Vandenbosch, S. L. Ooi, and N. H. M. Rais, "Design of a broadband all-textile slotted PIFA," *IEEE Transactions on Antennas and Propagation*, vol. 60, no. 1, pp. 379–384, 2012.

[18] *CST Microwave Studio*, CST-Computer Simulation Technology AG, Darmstadt, Germany, 2012.

[19] C. A. Balanis, *Antenna Theory Analysis and Design*, Wiley and Sons, New York, NY, USA, 3rd edition, 2005.

[20] P. B. Samal, P. J. Soh, and G. A. E. Vandenbosch, "A systematic design procedure for microstrip-based unidirectional UWB antennas," *Progress In Electromagnetics Research*, vol. 143, pp. 105–130, 2013.

[21] A. A. Abdelaziz, "Bandwidth enhancement of microstrip antenna," *Progress In Electromagnetics Research*, vol. 63, pp. 311–317, 2006.

[22] M. Koohestani and M. Golpour, "U-shaped microstrip patch antenna with novel parasitic tuning stubs for ultra wideband applications," *IET Microwaves, Antennas & Propagation*, vol. 4, no. 7, p. 938, 2010.

[23] M. Klemm, I. Z. Kovcs, G. F. Pedersen, and G. Troster, "Novel small-size directional antenna for UWB WBAN/WPAN applications," *IEEE Transactions on Antennas and Propagation*, vol. 53, no. 12, pp. 3884–3896, 2005.

[24] A. Dumoulin, M. J. Ammann, and P. McEvoy, "Performance evaluation of antennas for UWB radar and positioning systems," in *IET Irish Signals and Systems Conference (ISSC 2009)*, pp. 1–6, Dublin, Ireland, 2009.

[25] M. A. B. Abbasi, S. S. Nikolaou, M. A. Antoniades, M. Nikolić Stevanović, and P. Vryonides, "Compact EBG-backed planar monopole for BAN wearable applications," *IEEE Transactions on Antennas and Propagation*, vol. 65, no. 2, pp. 453–463, 2017.

[26] "IEC/IEEE International Standard—determining the peak spatial-average specific absorption rate (SAR) in the human body from wireless communications devices, 30 MHz to 6 GHz—part 1: general requirements for using the finite-difference time-domain (FDTD) method for SAR calculations," in *IEC/IEEE 62704-1:2017*, pp. 1–86, 2017.

[27] R. B. V. B. Simorangkir, S. M. Abbas, and K. P. Esselle, "A printed UWB antenna with full ground plane for WBAN applications," in *2016 International Workshop on Antenna Technology (iWAT)*, pp. 127–130, Cocoa Beach, FL, USA, 2016.

[28] L. A. Yimdjo Poffelie, P. J. Soh, S. Yan, and G. A. E. Vandenbosch, "A high-fidelity all-textile UWB antenna with low back radiation for off-body WBAN applications," *IEEE Transactions on Antennas and Propagation*, vol. 64, no. 2, pp. 757–760, 2016.

[29] K. Shikder and F. Arifin, "A novel UWB wearable icon-type textile antenna for WBAN applications," in *2017 International Conference on Electrical, Computer and Communication Engineering (ECCE)*, pp. 886–890, Cox's Bazar, Bangladesh, 2017.

[30] M. Ur-Rehman, Q. H. Abbasi, M. Akram, and C. Parini, "Design of band-notched ultra wideband antenna for indoor and wearable wireless communications," *IET Microwaves, Antennas & Propagation*, vol. 9, no. 3, pp. 243–251, 2015.